

**Correction of Density-Functional-Theory based polynomial
interatomic potentials to reproduce experimental melting
properties**

Bernd Bauerhenne* and Martin E. Garcia

Theoretical Physics and Center for Interdisciplinary Nanostructure

Science and Technology (CINSaT), University of Kassel,

Heinrich-Plett-Strasse 40, 34132 Kassel, Germany

(Dated: October 7, 2021)

arXiv:2110.02660v1 [cond-mat.mtrl-sci] 6 Oct 2021

Abstract

Recently, we developed a method to construct polynomial interatomic potentials from ab-initio calculations in order to accurately describe laser excited solids [PRL 124, 085501 (2020)]. However, ab-initio methods, and therefore analytical potentials derived from them, commonly do not provide an accurate prediction of the melting temperature. In order to reproduce the experimental melting properties, but keeping the accuracy in the laser excited case, we present here an approach to modify few key coefficients of polynomial interatomic potentials constructed from ab-initio data. We show that, with the help of such corrections, the electronic-temperature dependent interatomic potential for silicon can, at the same time, describe nonthermal laser induced effects with ab-initio accuracy and also provide the correct experimental melting temperature and slope dT/dp .

I. INTRODUCTION

Interatomic potentials allow for ultra-large scale atomistic molecular dynamics (MD) simulations with up to billions of atoms [1] and simulation times of nanoseconds, which is necessary to get insights into many physical processes, such as diffusion [2–4], plastic deformation [5, 6], melting [7, 8], crystallization [8, 9] and other phase transformations [10, 11]. Femtosecond laser pulses excite the electrons in matter to high electronic temperatures T_e 's inducing significant ultrafast changes in the interatomic bonding whereas the ions remain mostly unaffected until electron-phonon interactions become active [12]. In order to address the short lived changes in interatomic bonding due to the hot electrons in large scale MD simulations, T_e -dependent interatomic potentials were introduced [13–20], which depend beside the atomic coordinates also on the electronic temperature T_e . The hot electrons cause many ultrafast phenomena like bond hardening or softening [21–23], structural solid-solid and solid-liquid phase transitions [24–26], phonon squeezing or antisqueezing [27, 28], excitation of coherent phonons [29, 30], which can be well described by T_e -dependent density functional theory (DFT). Such ab-initio methods cannot access atomistic simulations on such large temporal and spatial dimensions as interatomic potentials can do. It has been shown in different works that one can use ab-initio methods to generate data for constructing interatomic potentials [31, 32]. However, an accurate prediction of the melting properties of

* bauerhenne@uni-kassel.de

solids is usually not feasible using ab-initio methods. In silicon (Si), for instance, DFT in the local density approximation (LDA) predicts a melting temperature of $T_m(p) = (1300 \pm 50) \text{ K} - 58 \frac{\text{K}}{\text{GPa}} \times p$ [33], which is 20 % below the experimental value of $T_m = (1687 \pm 5) \text{ K} - 58 \frac{\text{K}}{\text{GPa}} \times p$ [34, 35]. The usage of the generalized gradient approximation of Perdew-Burke-Ernzerhof (PBE) improves the prediction to $T_m(p) = (1492 \pm 50) \text{ K} - 42 \frac{\text{K}}{\text{GPa}} \times p$ [33]. But only the application of the random phase approximation (RPA) together with PBE yields the correct melting temperature [36]. Although compact analytical expressions exist for the interatomic forces within the RPA, the computation of the forces is extremely demanding [37]. Thus, in order to construct an accurate interatomic potential, it may be more efficient to generate the data from DFT without RPA, to fit these data to an interatomic potential and to modify afterwards the coefficients of the obtained interatomic potential for reproducing the experimental melting temperature. For example, this was done by Kumagai *et al.*, who developed an interatomic potential for Si with electrons in the ground state. The coefficients were firstly fitted to LDA-DFT data and then one coefficient was additionally modified to reach the experimental melting temperature [38]. Such a procedure may be even more appealing for constructing T_e -dependent interatomic potentials, since T_e -dependent DFT alone describes very well interatomic bonding at increased T_e and, therefore, is quite suitable to generate data for fitting.

We recently developed a T_e -dependent interatomic potential for Si [20] by fitting interatomic forces and structural energies from molecular dynamics simulations in thin-film geometry using T_e -dependent DFT in the local density approximation. The obtained interatomic potential describes, when included with atomistic simulations, femtosecond laser-induced effects in Si, like the bond softening, thermal phonon antisqueezing, non-thermal melting, and ablation with remarkable accuracy. The interatomic potential for Si has a melting temperature of $T_m(p) = (1199 \pm 2) \text{ K} - (40 \pm 3) \frac{\text{K}}{\text{GPa}} \times p$ which agrees with the LDA-DFT value but differs from the experimental one. Here we present a method to modify several coefficients of the T_e -dependent interatomic potential for Si at low T_e 's in such a way that the experimental melting temperature is reproduced, a negative slope in the melting temperature vs. pressure diagram is obtained, and that there are no significant changes in the description of the potential energy surface at high T_e 's.

The paper is organized as follows. At first we explain how we calculate the melting temperature and we describe the functional form of our derived T_e -dependent interatomic

potential for Si. Then, we introduce a modification of the three-body term of the potential that increases the melting temperature to the experimental value. But this modification causes an unphysical positive slope of the melting temperature as a function of pressure close to zero pressure. To correct this, we introduce a simple trial interatomic potential consisting of a two-body and a three-body potential like the, for instance, the terms present in the Stillinger & Weber potential [32]. We modify independently the strength of the two-body and the three-body potential and analyze the influence on the melting temperature and on the slope in the melting temperature vs. pressure curve. Using the insights learned from this study, we introduce a modification of the two-body and three-body potential of our T_c -dependent interatomic potential for Si that increases the melting temperature to the experimental value and induces a negative slope. Finally, we analyze the modified potential and show the influence of the modification on the physical properties compared to the original potential.

II. METHODS

A. Calculation of the melting temperature

We derive the ionic temperature of the ions using the equipartition theorem

$$T_i = \frac{2 E_{\text{kin}}}{3 N_{\text{at}} k_B}, \quad (1)$$

where E_{kin} is the kinetic energy of the ions, N_{at} is the number of atoms in the simulation cell and k_B is the Boltzmann constant. One cannot derive the melting temperature by just heating up the ideal bulk crystal structure or cooling down the liquid structure. Thus, we simulated the coexistence of liquid and crystal parts [39] to obtain reliably the melting temperature T_m . For this, we used a bulk simulation cell that consists of $32 \times 16 \times 16$ conventional cells and contains $N_{\text{at}} = 65536$ Si atoms. First we fixed the coordinates of half of the atoms and melted the other part of the crystal structure by applying the Anderson thermostat [40] at $T_i = 2500$ K. Then we allowed again a movement of all atoms. We applied the Anderson thermostat to all atoms at a temperature assumed to be close to the melting temperature. During this thermalization, the simulation cell volume and the atomic coordinates were scaled every picosecond to reach a given target pressure. We did three of such thermalizations in order to get the pressures $p = -1$ GPa, 0 GPa, 1 GPa. Using

the above mentioned procedure, we obtained an initialization of atomic coordinates and velocities at a given pressure and temperature. Half of the structure is molten and the other half is crystalline, so that two planar liquid-crystal interfaces exist within the simulation cell. Starting from this initialization, we performed a MD simulation at constant volume and energy for 500 ps using the Velocity Verlet algorithm [41]. We show a snapshot of the atomic structure at the initialization and one after the MD simulation period of 500 ps for the initialization at zero pressure in Fig. 1.

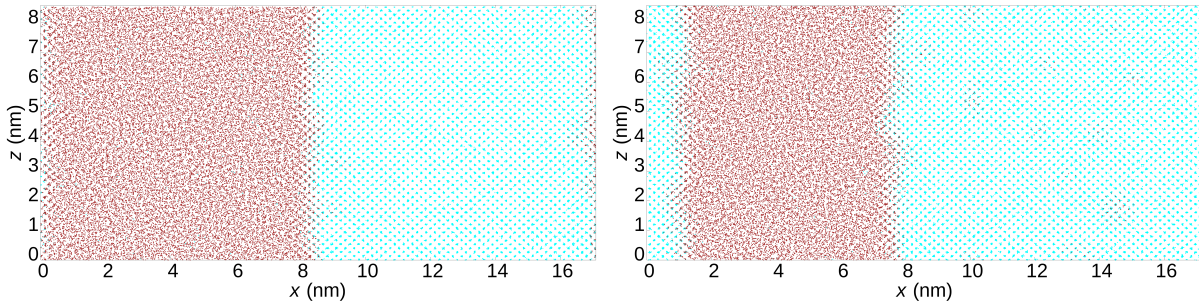


FIG. 1. Snapshots of the MD simulation with 65536 Si atoms at zero pressure are shown at the initialization $t = 0$ ps (top) and at $t = 500$ ps (bottom). The atoms are colored due to their CSP value [42]: cyan corresponds to crystalline and brown to molten environment.

In this MD simulation at constant energy (and volume), the ionic temperature T_i converges always to the melting temperature T_m . This can be explained as followed: If the initial temperature is below the melting temperature, the atoms of the liquid at the interface start to crystallize, so that the size of the liquid part is decreasing. This crystallization increases the temperature up to the melting temperature, because the heat of fusion is released from the crystallization. If the initial temperature is above the melting temperature, the atoms of the crystal at the interface start to melt, so that the size of the crystal part is decreasing. The melting decreases the temperature down to the melting temperature, because the heat of fusion is taken for the melting. In both cases the temperature converges to the melting temperature. If this temperature is reached, it remains constant, since the same amount of atoms melt and crystallize. Only small fluctuations occur, which decrease with the size of the simulation cell. We present the ionic temperature T_i obtained from Eq. (1) of the MD simulations at constant energy as a function of time for the original T_e -dependent interatomic Si potential in Fig. 2. One can clearly see, that T_i converges to the melting temperature at the given pressure and oscillates then around this value. One should be

aware that the temperature also remains constant in the end, if the whole structure melts or crystallizes in the MD simulation at constant energy, because the material remains then molten or crystalline. This occurs if one initializes the temperature to far away from the melting temperature. Therefore, we checked additionally the atomic structure, if there is really a coexistence of a liquid-crystal interface, as presented in Fig. 1.

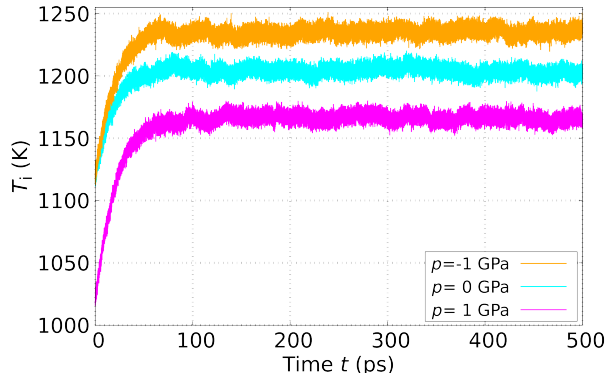


FIG. 2. Ionic temperatures occurring in the MD simulation of the bulk simulation cell with 65536 Si atoms are shown as a function of time for various constant pressures.

The fluctuations of the temperature, which occur after the melting temperature is reached, decrease with increasing simulation cell size. On the other hand, if the simulation cell is too small, the fluctuations are so large that the liquid-crystal interface cannot be stabilized, so that the whole structure always melts or crystallizes. We used this effect occurring in MD simulations of small simulation cells to derive an approximation of the melting temperature. For this, we set up a simulation cell consisting of $8 \times 4 \times 4$ conventional cells and containing $N_{\text{at}} = 1024$ Si atoms. In order to get bulk Si, we used periodic boundary conditions in all directions. At first, we fixed the atomic coordinates of half of the atoms and applied the Anderson thermostat at $T_i = 2500$ K to the unfixed atoms in order to melt their structure. By doing this, we obtained a structure, where half is molten and the other half is in a crystalline state. Then we allow all atoms to move and applied the Andersen thermostat at a given temperature T_i on a long timescale. Now the whole structure melts or crystallizes, as one can see in Fig. 3, where the structural energy is shown as a function of time for several temperatures.

The energy of the crystal phase is smaller compared to the energy of the liquid phase. Thus, the structural energy decreases, if the structure crystallizes entirely, and the structural

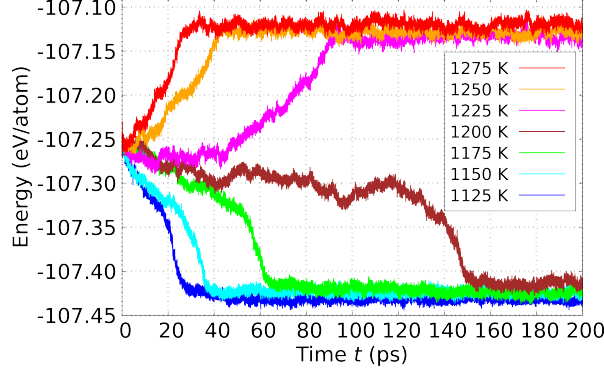


FIG. 3. The Helmholtz free energy in the MD simulation of the bulk simulation cell with 1024 Si atoms is shown as a function of time for various temperatures.

energy increases, if the structure melts entirely. If the temperature is chosen significantly below the melting temperature, the structure always crystallizes and, if the temperature is chosen significantly above the melting temperature, the structure always melts. If the temperature is chosen close to the melting temperature, the structure melts or crystallizes depending on the actually used random numbers in the Anderson thermostat. Due to this, one only obtains a rough approximation of the melting temperature from such simulations.

Since the melting temperature must be obtained from large-scale MD simulations of the liquid-crystal coexistence, it is obvious that one cannot directly fit the parameters of an interatomic potential to the value of the melting temperature.

B. Analytical form of the interatomic potential

We construct the T_e -dependent interatomic potential for Si [20] as a sum of a two-body potential Φ_2 , a three-body potential Φ_3 , an embedding function Φ_ρ and the Helmholtz free energy of an isolated Si atom Φ_0 :

$$\begin{aligned}
 \Phi = & \sum_{\substack{i < j \\ r_{ij} < r_2^{(c)}}} \Phi_2(T_e, r_{ij}) + \sum'_{\substack{i j k \\ r_{ij}, r_{ik} < r_3^{(c)}}} \Phi_3(T_e, r_{ij}, r_{ik}, \theta_{ijk}) \\
 & + \sum_i \Phi_\rho \left(T_e, \rho_i^{(2)}, \rho_i^{(3)}, \dots, \rho_i^{(N_\rho^{(r)})} \right) \\
 & + \sum_i \Phi_0(T_e).
 \end{aligned} \tag{2}$$

Here r_{ij} denotes the distance between atoms i and j , θ_{ijk} is the angle between \mathbf{r}_{ij} and \mathbf{r}_{ik} , the prime indicates that all summation indices are distinct, and $\rho_i^{(2)}$, $\rho_i^{(3)}$, \dots are different measures for the atomic density surrounding atom i (see below). $r_2^{(c)}$, $r_3^{(c)}$, and $r_\rho^{(c)}$ denote the individual cutoff radii for Φ_2 , Φ_3 , and Φ_ρ (see below), respectively. The different terms are constructed as

$$\Phi_2 = \sum_{q=2}^{N_2^{(r)}} c_2^{(q)} \left(1 - \frac{r_{ij}}{r_2^{(c)}} \right)^q, \quad (3)$$

$$\begin{aligned} \Phi_3 = & \sum_{q_1=2}^{N_3^{(r)}} \sum_{q_2=q_1}^{N_3^{(r)}} \sum_{q_3=0}^{N_3^{(\theta)}} c_3^{(q_1 q_2 q_3)} \times \\ & \times \left(1 - \frac{r_{ij}}{r_3^{(c)}} \right)^{q_1} \left(1 - \frac{r_{ik}}{r_3^{(c)}} \right)^{q_2} \left(\cos(\theta_{ijk}) \right)^{q_3}, \end{aligned} \quad (4)$$

$$\Phi_\rho = \sum_{q_1=2}^{N_\rho^{(r)}} \sum_{q_2=1}^{N_\rho^{(\rho)}} c_\rho^{(q_1 q_2)} \left(\frac{\rho_i^{(q_1)}}{1 + \rho_i^{(q_1)}} \right)^{q_2}, \quad (5)$$

and, for $q_1 = 2, 3, \dots, N_\rho^{(r)}$, the measures for the atomic density surrounding atom i are constructed as

$$\rho_i^{(q_1)} = \sum_{\substack{j \neq i \\ r_{ij} < r_\rho^{(c)}}} \left(1 - \frac{r_{ij}}{r_\rho^{(c)}} \right)^{q_1}. \quad (6)$$

The interatomic potential has the degrees

$$N_2^{(r)} = 10, \quad N_3^{(r)} = 3, \quad N_3^{(\theta)} = 3, \quad N_\rho^{(\rho)} = 2, \quad N_\rho^{(r)} = 2 \quad (7)$$

and needs in total 23 coefficients. The two-body potential Φ_2 has 9, the three-body potential Φ_3 has 12, and the embedding function Φ_ρ has 2 coefficients. Furthermore, the constant cutoff radii

$$r_2^{(c)} = 0.63 \text{ nm}, \quad r_3^{(c)} = 0.42 \text{ nm}, \quad r_\rho^{(c)} = 0.48 \text{ nm} \quad (8)$$

are used. The coefficients $\{c_2^{(q)}\}$, $\{c_3^{(q_1 q_2 q_3)}\}$, $\{c_\rho^{(q_1 q_2)}\}$ depend on T_e and are tabulated in the Supplemental Material of Ref. [20].

III. RESULTS AND DISCUSSION

A. Correction of the 3-body potential coefficients

In order to increase the melting temperature in the interatomic potential description, we have to stabilize the Si crystal, which forms the diamond-like structure. We mean by a stabilization of a structure that the bonding energy of this structure should become higher within the interatomic potential description. Each atom joins four nearest neighbors in the diamond-like structure. The angle θ_{ijk} between any of these neighbors is always equal and obeys $\cos(\theta_{ijk}) = -\frac{1}{3}$. Consequently, we should stabilize this angle for the nearest neighbors. We can easily do this done by adding the following correction term to the three-body potential:

$$\Phi_3^{(\text{cor})}(r_{ij}, r_{ik}, \theta_{ijk}) = g(r_{ij}) g(r_{ik}) \left(\cos(\theta_{ijk}) + \frac{1}{3} \right)^2, \quad (9)$$

with $g(r_{ij}) \geq 0$ and $g(r_{ik}) \geq 0$. This construction takes care that the preferred nearest neighbor angle of the diamond-like structure is stabilized by the parabola that exhibits its minimum at $-\frac{1}{3}$ for $\cos(\theta_{ijk})$. The distance function $g(r)$ should be constructed in such a way, that mainly the nearest neighbors are affected, which are located at a distance of 0.234 nm for Si.

In order to add a correction term like Eq. (9) to the three-body potential, we use the following construction, which just corresponds to a modification of three existing coefficients:

$$\begin{aligned} & \Phi_3^{(\text{cor})}(r_{ij}, r_{ik}, \theta_{ijk}) \\ &= \underbrace{\sqrt{\aleph_3} \left(1 - \frac{r_{ij}}{r_3^{(c)}} \right)^3}_{=g(r_{ij})} \underbrace{\sqrt{\aleph_3} \left(1 - \frac{r_{ik}}{r_3^{(c)}} \right)^3}_{=g(r_{ik})} \left(\cos(\theta_{ijk}) + \frac{1}{3} \right)^2 \\ &= \aleph_3 \left(1 - \frac{r_{ij}}{r_3^{(c)}} \right)^3 \left(1 - \frac{r_{ik}}{r_3^{(c)}} \right)^3 \left(\cos(\theta_{ijk}) \right)^2 \\ &+ \frac{2}{3} \aleph_3 \left(1 - \frac{r_{ij}}{r_3^{(c)}} \right)^3 \left(1 - \frac{r_{ik}}{r_3^{(c)}} \right)^3 \cos(\theta_{ijk}) \\ &+ \frac{1}{9} \aleph_3 \left(1 - \frac{r_{ij}}{r_3^{(c)}} \right)^3 \left(1 - \frac{r_{ik}}{r_3^{(c)}} \right)^3. \end{aligned} \quad (10)$$

The strength of the correction is controlled by \aleph_3 . $\aleph_3 = 0$ corresponds to the uncorrected

original potential. We selected the term $\left(1 - r/r_3^{(c)}\right)^3$ instead of $\left(1 - r/r_3^{(c)}\right)^2$, since power of three converges faster to zero at reaching the cutoff-radius of $r_3^{(c)} = 0.42$ nm and, consequently, the correction is more dominated at the nearest neighbor distance of 0.234 nm. Adding the above mentioned term to the potential corresponds to add $\frac{1}{9} \aleph_3$ to $c_3^{(330)}$, $\frac{2}{3} \aleph_3$ to $c_3^{(331)}$, and \aleph_3 to $c_3^{(332)}$. The potential correction should only take place at low electronic temperatures T_e around the experimental melting temperature $T_m = 1687$ K, since no modifications should be done at higher T_e 's. Thus, we did the following: We obtained the interatomic potential coefficients from a polynomial approximation of the fitted ideal coefficient values at the eleven electronic temperatures of 316 K (1 mHa), 3158 K (10 mHa), 6315 K (20 mHa), \dots , 31578 K (100 mHa). Consequently, we added the corresponding correction value to the ideal coefficient values for $c_3^{(330)}$, $c_3^{(331)}$, and $c_3^{(332)}$. Furthermore, we added the correction value at 316 K and added half of it at 3158 K, since the correction should only take place at low T_e 's and should smoothly vanish above the experimental melting temperature of $T_m = 1687$ K. Finally, we approximated the corrected polynomial from these at two low T_e 's shifted ideal coefficient values.

In order to demonstrate this procedure, we present the original and corrected ideal coefficient values together with the corresponding original and corrected polynomial in Fig. 4 for $\aleph_3 = 12$ eV, which leads to the experimental melting temperature. As expected, the corrected polynomial significantly differs from the original only at electronic temperatures below 7000 K.

We performed the above described correction of the interatomic potential at several values of \aleph_3 . We derived the melting temperature T_m for each corrected interatomic potential at the three pressures p of -1 GPa, 0 GPa, and 1 GPa. For this, we performed large scale liquid-crystal coexistence MD simulations using the simulation cell with 65536 atoms as described in Sec. II A. We determined the melting temperature T_m *vs.* pressure slope $\left.\frac{dT_m}{dp}\right|_{p=0}$ and melting temperature $T_m|_{p=0}$ at zero pressure from the obtained three T_m values by a linear regression. In TAB. I, we list the results of the linear regression.

An increasing \aleph_3 correction induces an increase of the melting temperature of the interatomic potential, as expected, and the experimental value is reached at $\aleph_3 = 12$ eV. However, an increasing \aleph_3 induces also an increase of the slope $\left.\frac{dT_m}{dp}\right|_{p=0}$ in the T_m *vs.* p diagram. The slope rises from -40 K/GPa at $\aleph_3 = 0$ up to 18 K/GPa at $\aleph_3 = 12$ eV (see TAB. I). The

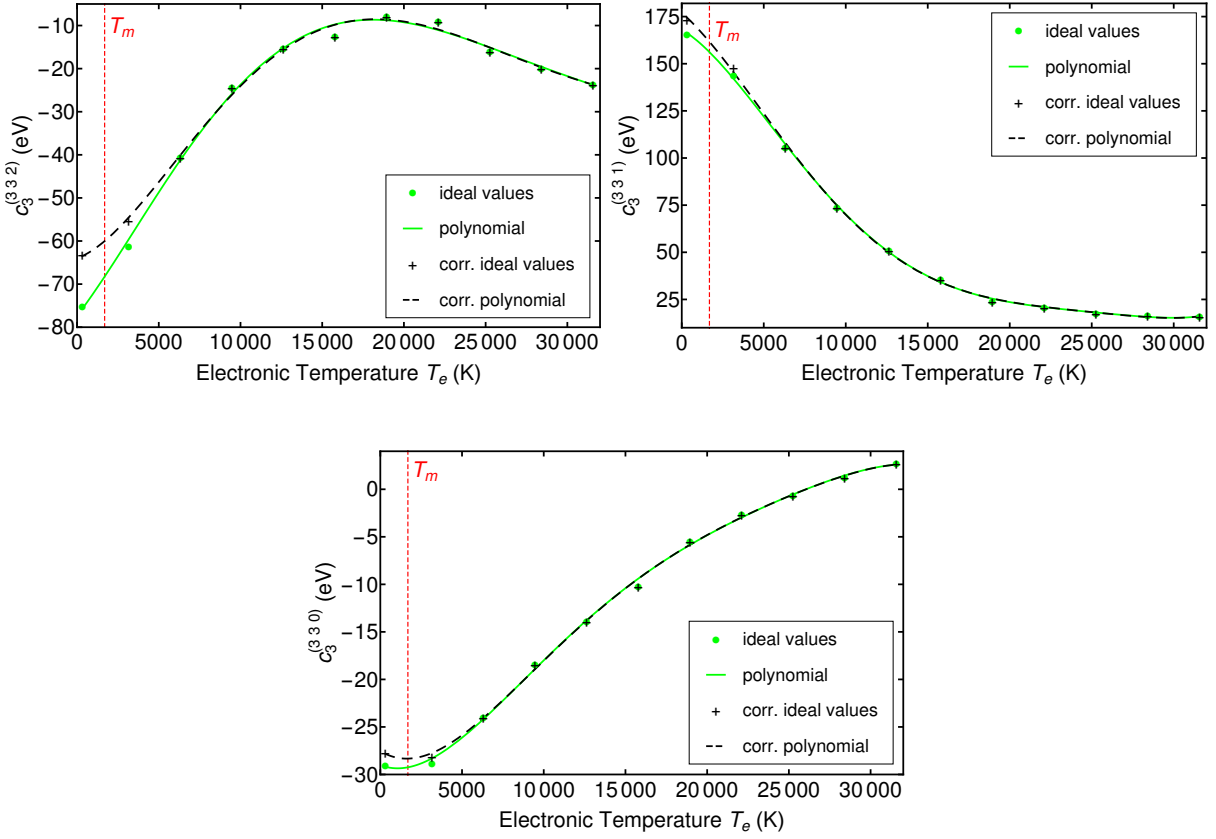


FIG. 4. The polynomial approximation of the potential coefficients $c_3^{(330)}$, $c_3^{(331)}$, and $c_3^{(332)}$ is shown together with the ideal values before (green) and after (black) the correction of the ideal values at $T_e = 316$ K and $T_e = 3158$ K. $N_3 = 12$ eV is shown, which yields the experimental melting temperature $T_m = 1687$ K highlighted by a red vertical line.

experimental value of the slope yields -58 K/GPa [35]. Consequently, we cannot accept the slope 18 K/GPa of the melting temperature corrected interatomic potential, because it is even positive compared to the experimental value.

In order to study how an interatomic potential must be modified to increase, on the one hand, the melting temperature and to get, on the other hand, a negative slope, we constructed and analyzed a series of test potentials. All of these test potentials exhibit the experimental melting temperature, but different slopes. The results of this study are reported in the next section.

TAB. I. Melting temperature $T_m|_{p=0}$ and slope $\left.\frac{dT_m}{dp}\right|_{p=0}$ in the T_m vs. p diagram near zero pressure are listed for different \aleph_3 -corrections of the interatomic potential coefficients. The listed errors have their origin in the standard deviation of the ionic temperature in the liquid-crystal coexistence MD simulations, because the error of the linear regression is much smaller.

\aleph_3 (eV)	$T_m _{p=0}$ (K)	$\left.\frac{dT_m}{dp}\right _{p=0}$ ($\frac{\text{K}}{\text{GPa}}$)
0.0	1199 ± 2	-40 ± 3
3.0	1388 ± 2	-12 ± 3
6.0	1514 ± 3	2 ± 3
9.0	1610 ± 3	11 ± 4
12.0	1687 ± 3	18 ± 4

B. Melting Temperature and slope study on test potentials

The widely used Stillinger & Weber potential [32] is the sum of a two-body potential $\Phi_2^{(\text{SW})}$ and a three-body potential $\Phi_3^{(\text{SW})}$. It exhibits the experimental melting temperature and a significantly negative slope. The three body potential is constructed like Eq. (9) with the distance function

$$g^{(\text{SW})}(r) = \sqrt{\frac{\lambda_0}{2}} \exp\left(\frac{\sigma}{r - r^{(c)}}\right)^\gamma. \quad (11)$$

It uses the cutoff radius $r^{(c)} = 0.377118$ nm and the parameters $\sigma = 0.20951$ nm, $\lambda_0 = 45.532305023389895$ eV, and $\gamma = 1.2$.

In order to construct a simple polynomial test potential $\Phi^{(\text{pol})}$ similar to the construction of the polynomial Si potential, we set it as a sum of a two-body and a three-body potential similar to the Stillinger & Weber potential. We construct the two-body potential as

$$\begin{aligned} \Phi_2^{(\text{pol})}(r_{ij}) = & -\frac{3\aleph_2 \left(r_2^{(c)}\right)^2}{\left(r_2^{(c)} - r^{(\text{min})}\right)^2} \left(1 - \frac{r_{ij}}{r_2^{(c)}}\right)^2 \\ & + \frac{2\aleph_2 \left(r_2^{(c)}\right)^3}{\left(r_2^{(c)} - r^{(\text{min})}\right)^3} \left(1 - \frac{r_{ij}}{r_2^{(c)}}\right)^3 \end{aligned} \quad (12)$$

and we construct the three-body potential following Eq. (9) using the simple distance

function

$$g^{(\text{pol})}(r) = \sqrt{\aleph_3} \left(1 - \frac{r}{r_3^{(\text{c})}} \right)^2. \quad (13)$$

Using this construction, $\Phi_2^{(\text{pol})}$ exhibits one single minimum, which is reached at $r^{(\text{min})}$ and has got the value of $-\aleph_2$. We set the position of the minimum to $r^{(\text{min})} = 0.234$ nm, which is the distance between the nearest neighbors in Si.

As a starting point of our study, we set the strength $\aleph_2 = 2.18$ eV and the cutoff-radius $r_2^{(\text{c})} = 0.35$ nm to get a similar course of the polynomial two-body potential $\Phi_2^{(\text{pol})}$ compared with the Stillinger & Weber two-body potential $\Phi_2^{(\text{SW})}$ for distances bigger than the first neighbor distance 0.234 nm, as one can see in Fig. 5.

We varied the strength \aleph_3 of the corresponding three-body potential $\Phi_3^{(\text{pol})}$ in order to get the same melting temperature at zero pressure like the Stillinger & Weber potential. In this way we found $\aleph_3 = 71.2336$ eV and, for this value, $g^{(\text{pol})}(r)$ is similar to $g^{(\text{SW})}(r)$ for distances bigger than 0.25 nm, as one can see in FIG. 6. To determine \aleph_3 , we initially performed several small cell liquid-crystal coexistence MD simulations to get a prediction of the corresponding \aleph_3 value. Then we performed large scale liquid-crystal coexistence MD simulations for a few \aleph_3 values to get the searched value of $\aleph_3 = 71.2336$ eV. We repeated this whole procedure for several strengths \aleph_2 of the polynomial two-body potential to get the corresponding \aleph_3 values for reaching the same melting temperature at zero pressure. We also reduced the cutoff-radius of the polynomial two-body potential to $r_2^{(\text{c})} = 0.33$ nm at $\aleph_2 = 2.18$ eV and determined the corresponding \aleph_3 . We list the obtained results in Tab. II. In addition, we increased the cutoff-radius of the polynomial two-body potential to $r_2^{(\text{c})} = 0.37$ nm at $\aleph_2 = 2.18$ eV. But this setting leads to a crystallization in the hexagonal closed-packed (hcp) structure instead of the diamond-like structure. Consequently, we skipped this parameter combination in Tab. II.

Our study shows that the strength \aleph_2 of the two-body potential is not relevant for the melting temperature $T_m|_{p=0}$ at zero pressure, as one can be seen in Tab. II. Rather, $T_m|_{p=0}$ is defined by the relationship of \aleph_2 and \aleph_3 . Fig. 7 shows $\sqrt{\aleph_3}$ as a function of \aleph_2 for the test potentials with $r_2^{(\text{c})} = r_3^{(\text{c})} = 0.35$ nm and $T_m|_{p=0} \approx 1687$ K. All these values lie on a straight line, which can be obtained from a linear regression. In order to reach the same melting temperature, \aleph_3 has to increase quadratically for increasing \aleph_2 and \aleph_3 has to decrease quadratically for decreasing \aleph_2 . It is obvious that this dependence is only valid in

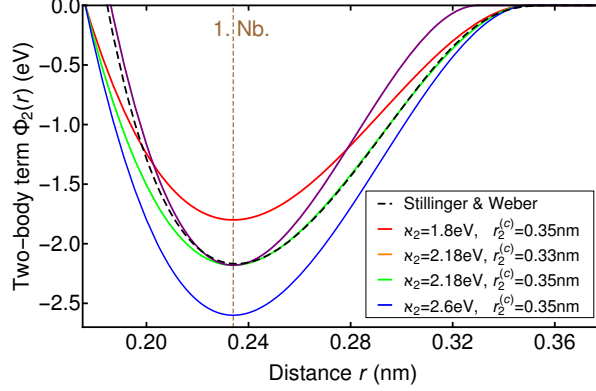


FIG. 5. The two-body potential $\Phi_2^{(SW)}$ of Stillinger & Weber is shown together with the two-body potentials $\Phi_2^{(pol)}$ of selected test potentials. The brown vertical line indicates the distance of the nearest neighbors in Si.

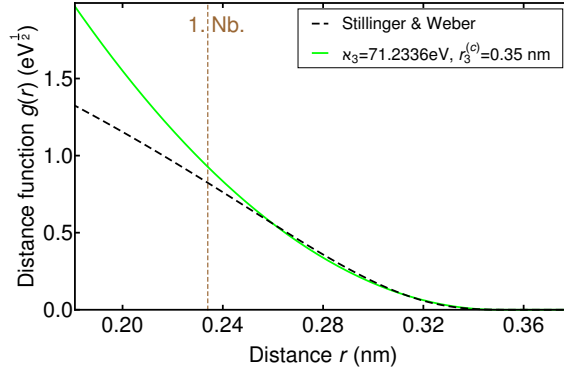


FIG. 6. Distance function $g(r)$ of the Stillinger & Weber and the test potential with $\Phi_2^{(SW)} \approx \Phi_2^{(pol)}$ and same T_m is shown. The brown vertical line indicates the distance of the nearest neighbors in Si.

a certain interval for \aleph_2 , since the nearest neighbor distance is not stabilized any more for $\aleph_2 \rightarrow 0$ and the crystal will melt easily at very low temperatures.

The two-body potential is responsible that the nearest neighbors are located at the distance, which corresponds to its minimum. If no three-body potential is present, each atom prefers as much neighbors as possible at this distance, which is fulfilled for a closed-packed structure like fcc or hcp. But the presence of the three-body potential forces the nearest neighbors to exhibit always an angle θ obeying $\cos(\theta) = -\frac{1}{3}$. This condition is only possible for four nearest neighbors building a tetragonal structure. Consequently, the diamond-like

TAB. II. Melting temperature $T_m|_{p=0}$ and slope $\frac{dT_m}{dp}|_{p=0}$ at zero pressure are listed for the different test and the Stillinger & Weber potential.

\aleph_2 (eV)	\aleph_3 (eV)	$r_2^{(c)}$ (nm)	$r_3^{(c)}$ (nm)	$T_m _{p=0}$ (K)	$\frac{dT_m}{dp} _{p=0}$ ($\frac{\text{K}}{\text{GPa}}$)
Stillinger & Weber	0.377118	0.377118	0.377118	1688 ± 3	-49 ± 3
1.8	61.999876	0.35	0.35	1689 ± 3	-29 ± 4
2.0	66.7489	0.35	0.35	1688 ± 3	-43 ± 3
2.18	71.2336	0.35	0.35	1689 ± 3	-56 ± 4
2.2	71.723961	0.35	0.35	1687 ± 3	-58 ± 4
2.4	76.9831	0.35	0.35	1689 ± 3	-68 ± 3
2.6	82.337476	0.35	0.35	1689 ± 3	-89 ± 3
2.18	45.104656	0.33	0.35	1688 ± 3	-80 ± 6

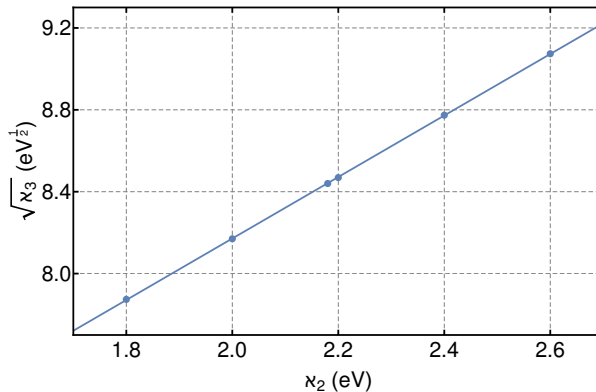


FIG. 7. $\sqrt{\aleph_3}$ is shown as a function of \aleph_2 for the test potentials with $r_2^{(c)} = r_3^{(c)} = 0.35$ nm and $T_m \approx 1687$ K (see TAB. II). Also a linear regression line is inserted.

structure is formed, which is called open, because free space exists between the atoms, to which the atoms could move during melting. In addition, if the cutoff radius of the two-body potential is bigger than that one of the three-body potential, the atoms still crystallize in the hcp structure like it would be without three-body potential.

An increase of the pressure p induces a closer location of the atoms to each other. Now, the nearest neighbors are located to close to each other and the two-body potential associated forces move them further away. Consequently, the nearest neighbors can move more easily

into the free space and the crystal will melt more easily, *i.e.*, T_m decreases with increasing pressure. On the other hand, a decrease of the pressure induces bigger distances between the atoms. Then, the nearest neighbors are located to far away to each other and the two-body potential associated forces move them closer together. Consequently, the nearest neighbors can move less easily into the free space and the crystal will melt more hardly, *i.e.*, T_m increases with decreasing pressure. This is the explanation of the negative slope.

Moreover, a bigger increase besides the minimum of the two-body potential, like for increasing \aleph_2 or decreasing $r_2^{(c)}$ (see Tab. II), induces a more negative slope, because the pressure-conditioned displacement of the nearest neighbors from their equilibrium distance will cause stronger forces on them. Hence, we should add a function with a minimum at the nearest neighbor distance and a strong increase beside this minimum to the two-body potential of the polynomial Si potential in order to achieve a negative slope.

C. Correction of the 2-body and 3-body potential coefficients

If we use the previous results, we need to modify the two- and three-body potentials of the polynomial Si potential $\Phi^{(\text{Si})}(T_e)$ to control the melting temperature $T_m|_{p=0}$ and the slope $\frac{dT_m}{dp}|_{p=0}$ at zero pressure. Using \aleph_3 , we performed the manipulation of the three-body potential in exactly the same way as described in Sec. III A. The two-body potential of $\Phi^{(\text{Si})}(T_e)$ contains the cutoff-radius of $r_2^{(c)} = 0.63$ nm and has the degree $N_2^{(r)} = 10$ (see Sec. II B).

In order to get a negative slope, the coefficients $\{c_2^{(q)}\}$ of the two-body potential should be modified in the following way: A correction two-body term $\Phi_2^{(\text{cor})}$ should be added, which exhibits a single minimum at the nearest neighbor distance 0.234 nm of the diamond-like structure of Si and which increases strongly beside the minimum. To do do, we used a linear combination of the three highest powers of the term $(1 - r_{ij}/r_2^{(c)})$ for $\Phi_2^{(\text{cor})}$. The three highest powers were chosen for the manipulation, since lower powers induce a weaker increase beside the minimum of $\Phi_2^{(\text{cor})}$. We derive the coefficients of $\Phi_2^{(\text{cor})}$ from the following conditions: $\Phi_2^{(\text{cor})}$ exhibits a minimum at $r^{(\text{min})} = 0.234$ nm and sets to $-\aleph_2$ at this minimum and sets to zero at $r^{(1)} = 0.4$ nm. We introduce the last constraint, since $\Phi_2^{(\text{cor})}$ should stay approximately at 0 for distances between $r^{(1)}$ and the cutoff radius $r_2^{(c)} = 0.63$ nm. $r^{(1)}$ should be as small as possible, because the increase beside the minimum becomes bigger

for decreasing $r^{(1)}$, which allows a stronger slope $\left. \frac{dT_m}{dp} \right|_{p=0}$ control. But, if $r^{(1)}$ becomes smaller than 0.4 nm, $\Phi_2^{(\text{cor})}$ becomes significantly positive for distances bigger than $r^{(1)}$, which should be avoided. We present the correction two-body term $\Phi_2^{(\text{cor})}$, which fulfills the above mentioned conditions, in Fig. 8. It is constructed as

$$\begin{aligned} \Phi_2^{(\text{cor})}(r_{ij}) = & 647.3458562015724 \aleph_2 \left(1 - \frac{r_{ij}}{r_2^{(c)}} \right)^8 \\ & - 2712.579093531517 \aleph_2 \left(1 - \frac{r_{ij}}{r_2^{(c)}} \right)^9 \\ & + 2573.178456073968 \aleph_2 \left(1 - \frac{r_{ij}}{r_2^{(c)}} \right)^{10}. \end{aligned} \quad (14)$$

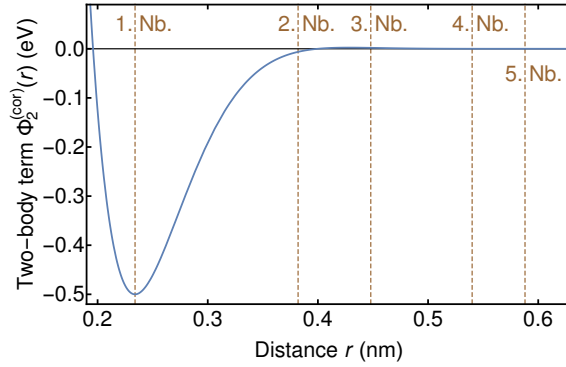


FIG. 8. The correction two-body term $\Phi_2^{(\text{cor})}$ is shown for $\aleph_2 = 0.5$ eV. The brown vertical lines indicate the positions of the neighbors in the diamond-like structure of Si.

Adding the above mentioned correction two-body term $\Phi_2^{(\text{cor})}$ to Φ_2 corresponds just to modify the coefficients $c_8^{(2)}$, $c_9^{(2)}$ and $c_{10}^{(2)}$ of Φ_2 . More detailed, $647.3458562015724 \aleph_2$ is add to $c_2^{(8)}$, $-2712.579093531517 \aleph_2$ to $c_2^{(9)}$ and $2573.178456073968 \aleph_2$ to $c_2^{(10)}$.

Similar to the \aleph_3 modification, we add the corresponding correction value to the ideal coefficient values at $T_e = 316$ K and half of it at $T_e = 3158$ K before the polynomial is approximated from the ideal coefficient values in order to get the smooth T_e -dependence of the potential coefficients. We show in Fig. 9 the original and corrected ideal coefficient values together with the corresponding fitted polynomials for the modified coefficients at $\aleph_2 = 0.5$ eV and $\aleph_3 = 20.3$ eV.

We gradually increased \aleph_2 and, for each \aleph_2 , we determined the corresponding \aleph_3 in such a way that the interatomic potential exhibits the experimental melting temperature of

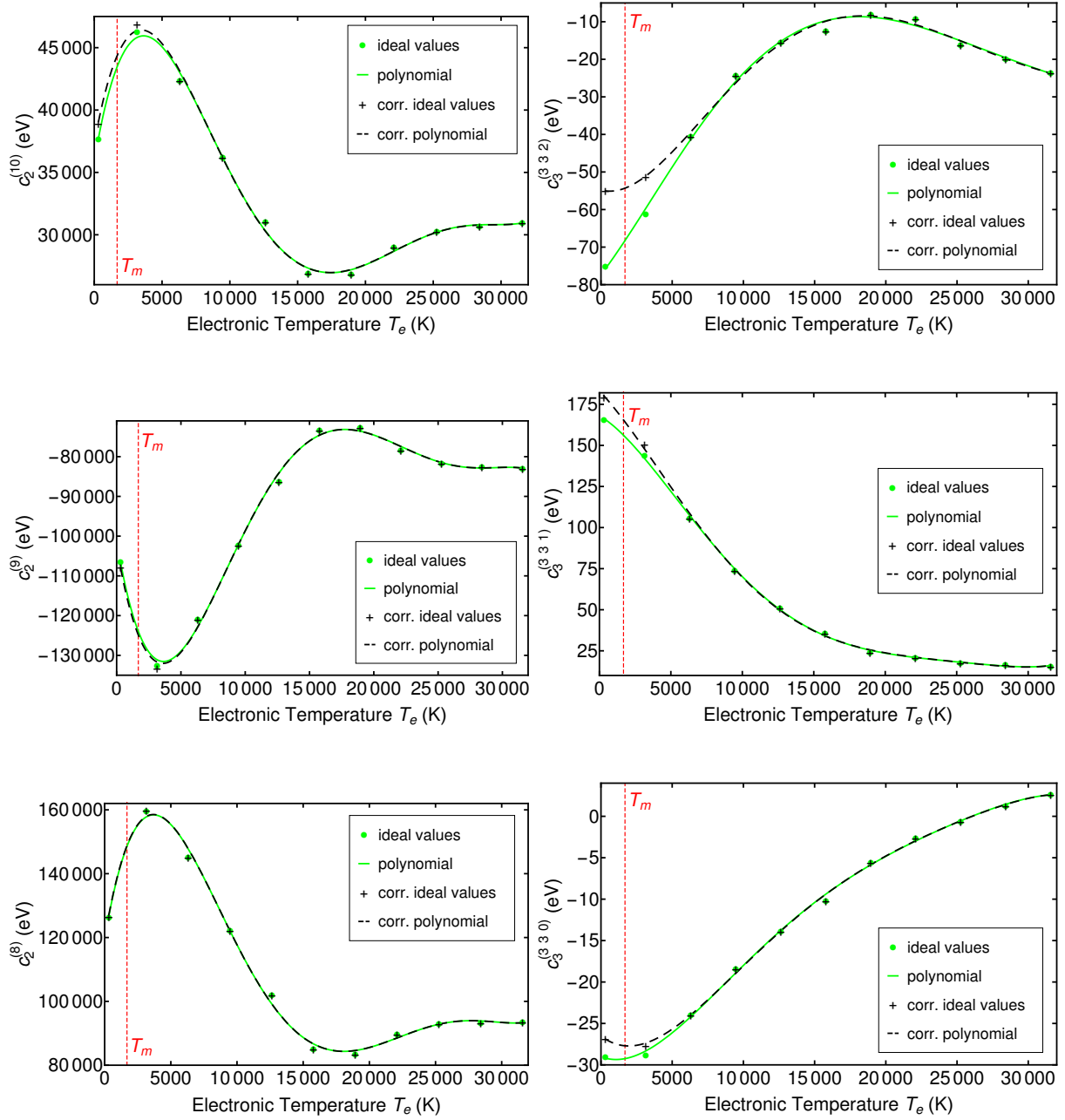


FIG. 9. The polynomial approximation of the coefficients $c_8^{(2)}$, $c_9^{(2)}$, $c_{10}^{(2)}$, $c_{330}^{(3)}$, $c_{331}^{(3)}$, and $c_{332}^{(3)}$ is shown together with the ideal values before (green) and after (black) the correction of the ideal values at $T_e = 316$ K and $T_e = 3158$ K. $\aleph_2 = 0.5$ eV and $\aleph_3 = 20.3$ eV are shown, which yields the experimental melting temperature $T_m = 1687$ K highlighted by a red vertical line.

$T_m = 1687$ K at zero pressure. For this, we used the procedure described in Sec. III B. In Summary, this study was very computational expensive and needed millions of core hours,

which were distributed on three different computer clusters. We list the finally obtained \aleph_2 , \aleph_3 pairs together with the corresponding melting temperature and slope at zero pressure in Tab. III.

TAB. III. Melting temperature $T_m|_{p=0}$ and slope $\frac{dT_m}{dp}|_{p=0}$ at zero pressure are listed for the different coefficient corrections to the interatomic potential.

\aleph_2 (eV)	\aleph_3 (eV)	$T_m _{p=0}$ (K)	$\frac{dT_m}{dp} _{p=0}$ ($\frac{\text{K}}{\text{GPa}}$)
0.0	12.0	1687 ± 3	18 ± 4
0.1	13.1	1686 ± 3	12 ± 4
0.2	14.6	1687 ± 3	3 ± 4
0.3	16.4	1689 ± 3	-1 ± 4
0.4	18.2	1685 ± 3	-7 ± 4
0.5	20.3	1689 ± 3	-11 ± 4
0.6	22.4	1688 ± 3	-14 ± 4

One can clearly see in Tab. III that the slope decreases with increasing \aleph_2 and it becomes negative at $\aleph_2 = 0.3$ eV. With increasing \aleph_2 value, also the phonon frequencies increase, since the bonding becomes stronger. At $\aleph_2 = 0.5$ eV, the corresponding phonon bandstructure of the diamond-like structure at $T_e = 316$ K looks similar to the one of the famous Stillinger & Weber potential, as one can be seen in Fig. 12. Especially the acoustic phonon branches are in an excellent agreement. Consequently, we selected $\aleph_2 = 0.5$ eV for the final corrected interatomic potential. We tabulate the corresponding modified coefficients in the Supplemental Material. In addition, we provide a Fortran subroutine for the calculation of the cohesive energy and the forces from the final corrected interatomic potential.

Fig. 10 presents the comparison of the phonon bandstructure, Fig. 11 the comparison of the cohesive energies of several bulk crystal structures, Fig. 14 the comparison of the absorbed electronic energy, and Fig. 13 the comparison of the electronic specific heat between the corrected and uncorrected interatomic potential at $T_e = 316$ K. The absorbed energy U_e and the electronic specific heat are directly calculated from the T_e -dependent interatomic

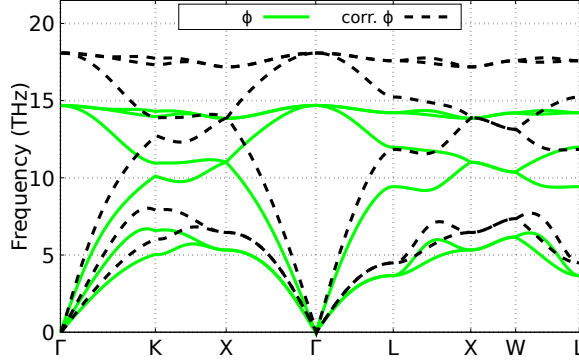


FIG. 10. The phonon bandstructure of the diamond-like structure is shown for the $\aleph_2 = 0.5$ eV, $\aleph_3 = 20.3$ eV corrected (black dashed) and uncorrected (green solid) interatomic potential Φ at $T_e = 316$ K.

potential from

$$U_e = \Phi - T_e \frac{\partial \Phi}{\partial T_e} \quad (15)$$

$$C_e = -T_e \frac{\partial^2 \Phi}{\partial T_e^2}. \quad (16)$$

The corrected potential contains a stronger two-body term. Thus, the phonon frequencies and the absolute value of the cohesive energies increase after the modification. The T_e -dependence of the electronic specific heat is significantly changed by the modification. We can still accept it, since it is positive. The absorbed electronic energy of the corrected interatomic potential is ~ 1.0 eV higher compared to the uncorrected one for $T_e > 10000$ K, but the functional shape is the same.

Among the data used for fitting, we included ab-initio structural free cohesive energies and ab-initio atomic forces from atomic configurations of molecular dynamics simulations at constant T_e . We also calculated the relative error in the atomic forces and the structural free cohesive energies of the atomic configurations from these molecular dynamics simulations for the corrected interatomic potential and compared it with the uncorrected one in Tab. IV. The correction does not induce any significant changes in the relative errors at high electronic temperatures $T_e \geq 9473$ K. This is not surprising, because the corrected polynomial does not differ from the uncorrected polynomial for the smooth T_e -approximation of the coefficients at high T_e 's, as it can be seen in Fig. 9. Consequently, the melting temperature correction does not influence the physical properties at high T_e .

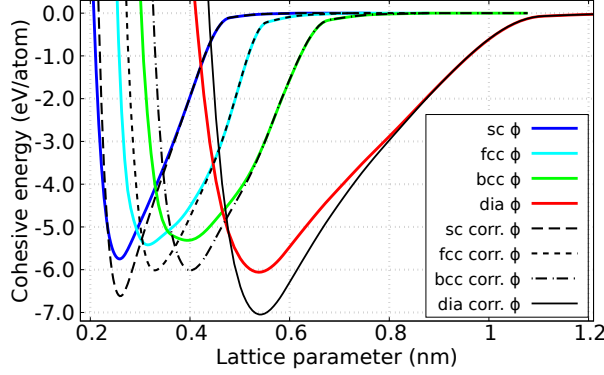


FIG. 11. The cohesive energies of different structures are shown for the $\aleph_2 = 0.5$ eV, $\aleph_3 = 20.3$ eV corrected (black dashed) and uncorrected (colored solid) interatomic potential Φ at $T_e = 316$ K.

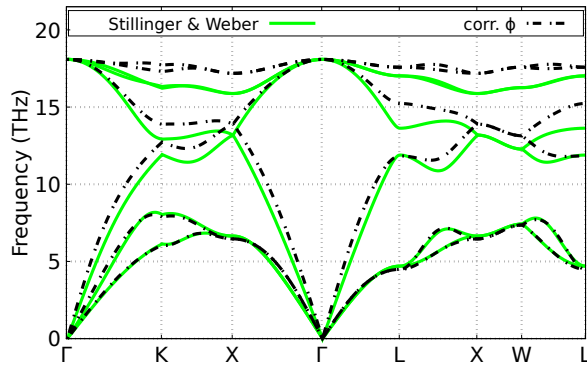


FIG. 12. The phonon bandstructure of the diamond-like structure is shown for the $\aleph_2 = 0.5$ eV, $\aleph_3 = 20.3$ eV corrected Φ at $T_e = 316$ K (black dot-dashed) and the Stillinger & Weber potential (green solid).

IV. CONCLUSIONS

We presented a modification of the coefficients of the two-body and three-body potential of our T_e -dependent interatomic potential for Si of Ref. [20] that increase the melting temperature to the experimental value of $T_m = 1687$ K [35] while maintaining a negative slope in the melting temperature vs. pressure diagram. The modification of only the coefficients of the three-body potential allows to increase the melting temperature to the experimental value but induces an unphysical positive slope. Thus, also the coefficients of the two-body potential must be modified, which induces finally a negative slope. The final corrected interatomic potential exhibits still a physically meaningful electronic specific heat and the

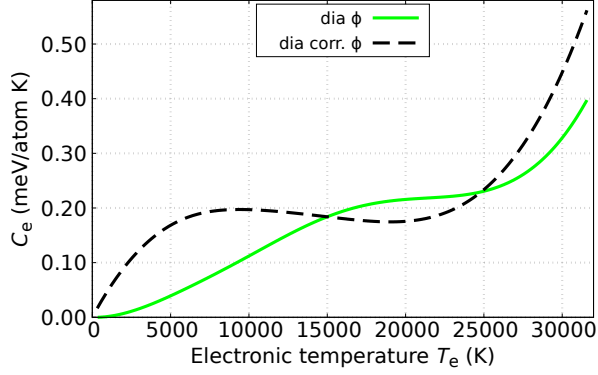


FIG. 13. The electronic specific heat C_e of the diamond-like structure is shown for the $\aleph_2 = 0.5$ eV, $\aleph_3 = 20.3$ eV corrected (black dashed) and uncorrected (green solid) interatomic potential Φ at $T_e = 316$ K.

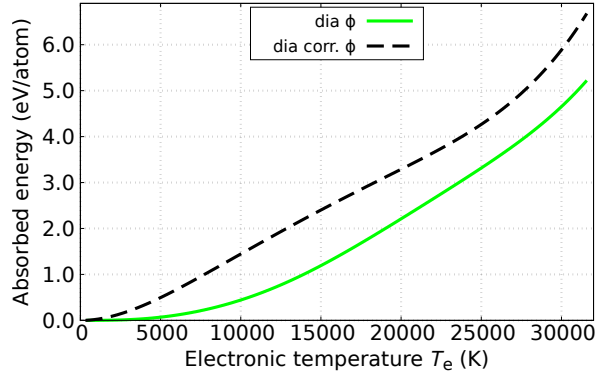


FIG. 14. The absorbed electronic energy E_{abs} of the diamond-like structure is shown for the $\aleph_2 = 0.5$ eV, $\aleph_3 = 20.3$ eV corrected (black dashed) and uncorrected (green solid) interatomic potential Φ at $T_e = 316$ K.

physical properties at high T_e 's are not influenced.

We want to point out that such a modification of the coefficients is impossible for the commonly used machine learning potentials like neural networks. Only the construction of the interatomic potential as a sum of physically interpretable terms together with the simple functional form of these terms allow such an adjustment of features that cannot be directly fitted.

TAB. IV. Relative error in the atomic forces f_{err} and in the structural free cohesive energies E_{err} of the molecular dynamics simulation are listed for the uncorrected and the $\aleph = 0.5$ eV, $\aleph_3 = 20.3$ eV corrected interatomic potential.

T_e (K)	$\aleph_2 = 0.5$ eV			
	uncorrected		$\aleph_3 = 20.3$ eV	
	f_{err} (%)	E_{err} (%)	f_{err} (%)	E_{err} (%)
316	25.8	1.1	65.7	14.6
3158	20.5	0.7	32.0	6.9
6315	13.9	0.4	14.7	1.7
9473	9.8	0.3	10.0	0.9
12631	7.7	0.5	8.2	1.6
15789	7.3	0.8	7.5	1.1
18946	11.2	0.6	11.2	0.2
22104	8.9	0.2	9.0	1.0
25262	6.6	0.6	6.6	0.6
28420	6.3	1.6	6.4	4.3
31577	6.6	1.1	6.6	2.9

ACKNOWLEDGMENTS

This work was supported by the DFG through the grant GA 465/15-2. B.B. acknowledges the support by the "Promotionsstipendium des Otto-Braun Fonds" and by the "Abschlussstipendium der Universität Kassel". Computations were performed on the Lichtenberg High Performance Computer (HHLR) TU Darmstadt, on the IT Servicecenter (ITS) University of Kassel, and on the computing cluster FUCHS University of Frankfurt.

-
- [1] Y. Shibuta, S. Sakane, E. Miyoshi, S. Okita, T. Takaki, and M. Ohno, Heterogeneity in homogeneous nucleation from billion-atom molecular dynamics simulation of solidification of pure metal, *Nature Communications* **8**, 10 (2017).
- [2] B. Cheng, A. T. Paxton, and M. Ceriotti, Hydrogen diffusion and trapping in α -iron: The

- role of quantum and anharmonic fluctuations, *Phys. Rev. Lett.* **120**, 225901 (2018).
- [3] G. B. Sushko, A. V. Verkhovtsev, A. V. Yakubovich, S. Schramm, and A. V. Solov'yov, Molecular dynamics simulation of self-diffusion processes in titanium in bulk material, on grain junctions and on surface, *The Journal of Physical Chemistry A* **118**, 6685 (2014).
- [4] J. J. Hoyt, M. Asta, and B. Sadigh, Test of the universal scaling law for the diffusion coefficient in liquid metals, *Phys. Rev. Lett.* **85**, 594 (2000).
- [5] A. V. Verkhovtsev, A. V. Yakubovich, G. B. Sushko, M. Hanauske, and A. V. Solov'yov, Molecular dynamics simulations of the nanoindentation process of titanium crystal, *Computational Materials Science* **76**, 20 (2013), selected Publications of the EU FP7 project VIRTUAL NANOTITANIUM (VINAT) "Theoretical analysis and virtual testing of titanium-based nano-materials".
- [6] M. Zink, K. Samwer, W. L. Johnson, and S. G. Mayr, Plastic deformation of metallic glasses: Size of shear transformation zones from molecular dynamics simulations, *Phys. Rev. B* **73**, 172203 (2006).
- [7] C. L. Cleveland, W. D. Luedtke, and U. Landman, Melting of gold clusters: Icosahedral precursors, *Phys. Rev. Lett.* **81**, 2036 (1998).
- [8] Y. Qi, T. Çağın, W. L. Johnson, and W. A. Goddard, Melting and crystallization in nanoclusters: The mesoscale regime, *The Journal of Chemical Physics* **115**, 385 (2001).
- [9] A. V. Yakubovich, G. Sushko, S. Schramm, and A. V. Solov'yov, Kinetics of liquid-solid phase transition in large nickel clusters, *Phys. Rev. B* **88**, 035438 (2013).
- [10] C. Kexel, S. Schramm, and A. V. Solov'yov, Atomistic simulation of martensite-austenite phase transition in nanoscale nickel-titanium crystals, *The European Physical Journal B* **9**, 221 (2015).
- [11] G. P. P. Pun and Y. Mishin, Molecular dynamics simulation of the martensitic phase transformation in NiAl alloys, *Journal of Physics: Condensed Matter* **22**, 395403 (2010).
- [12] P. Stampfli and K. H. Bennemann, Theory for the instability of the diamond structure of si, ge, and c induced by a dense electron-hole plasma, *Phys. Rev. B* **42**, 7163 (1990).
- [13] S. Khakshouri, D. Alfè, and D. M. Duffy, Development of an electron-temperature-dependent interatomic potential for molecular dynamics simulation of tungsten under electronic excitation, *Phys. Rev. B* **78**, 224304 (2008).
- [14] S. T. Murphy, S. L. Daraszewicz, Y. Giret, M. Watkins, A. L. Shluger, K. Tanimura, and D. M.

- Duffy, Dynamical simulations of an electronically induced solid-solid phase transformation in tungsten, *Phys. Rev. B* **92**, 134110 (2015).
- [15] G. E. Norman, S. V. Starikov, and V. V. Stegailov, Atomistic simulation of laser ablation of gold: Effect of pressure relaxation, *Journal of Experimental and Theoretical Physics* **114**, 792 (2012).
- [16] J. A. Moriarty, R. Q. Hood, and L. H. Yang, Quantum-mechanical interatomic potentials with electron temperature for strong-coupling transition metals, *Phys. Rev. Lett.* **108**, 036401 (2012).
- [17] L. Shokeen and P. K. Schelling, An empirical potential for silicon under conditions of strong electronic excitation, *Appl. Phys. Lett.* **97**, 151907 (2010).
- [18] L. Shokeen and P. K. Schelling, Thermodynamics and kinetics of silicon under conditions of strong electronic excitation, *J. Appl. Phys.* **109**, 073503 (2011).
- [19] R. Darkins, P.-W. Ma, S. T. Murphy, and D. M. Duffy, Simulating electronically driven structural changes in silicon with two-temperature molecular dynamics, *Phys. Rev. B* **98**, 024304 (2018).
- [20] B. Bauerhenne, V. P. Lipp, T. Zier, E. S. Zijlstra, and M. E. Garcia, Self-learning method for construction of analytical interatomic potentials to describe laser-excited materials, *Phys. Rev. Lett.* **124**, 085501 (2020).
- [21] V. Recoules, J. Cl  rouin, G. Z  rah, P. M. Anglade, and S. Mazevet, Effect of intense laser irradiation on the lattice stability of semiconductors and metals, *Phys. Rev. Lett.* **96**, 055503 (2006).
- [22] N. S. Grigoryan, T. Zier, M. E. Garcia, and E. S. Zijlstra, Ultrafast structural phenomena: theory of phonon frequency changes and simulations with code for highly excited valence electron systems, *J. Opt. Soc. Am. B* **31**, C22 (2014).
- [23] D. M. Fritz, D. A. Reis, B. Adams, R. A. Akre, J. Arthur, C. Blome, P. H. Bucksbaum, A. L. Cavalieri, S. Engemann, S. Fahy, R. W. Falcone, P. H. Fuoss, K. J. Gaffney, M. J. George, J. Hajdu, M. P. Hertlein, P. B. Hillyard, M. Horn-von Hoegen, M. Kammler, J. Kaspar, R. Kienberger, P. Krejcik, S. H. Lee, A. M. Lindenberg, B. McFarland, D. Meyer, T. Montagne,   . D. Murray, A. J. Nelson, M. Nicoul, R. Pahl, J. Rudati, H. Schlarb, D. P. Siddons, K. Sokolowski-Tinten, T. Tschentscher, D. von der Linde, and J. B. Hastings, Ultrafast bond softening in bismuth: Mapping a solid's interatomic potential with x-rays, *Science* **315**, 633

- (2007).
- [24] A. Cavalleri, C. Tóth, C. W. Siders, J. A. Squier, F. Ráksi, P. Forget, and J. C. Kieffer, Femtosecond structural dynamics in VO₂ during an ultrafast solid-solid phase transition, *Phys. Rev. Lett.* **87**, 237401 (2001).
 - [25] G. Sciaini, M. Harb, S. G. Kruglik, T. Payer, C. T. Hebeisen, F.-J. M. z. Heringdorf, M. Yamaguchi, M. H.-v. Hoegen, R. Ernstorfer, and R. J. D. Miller, Electronic acceleration of atomic motions and disordering in bismuth, *Nature* **458**, 56 (2009).
 - [26] M. Buzzi, M. Först, R. Mankowsky, and A. Cavalleri, Probing dynamics in quantum materials with femtosecond x-rays, *Nature Reviews Materials* **3**, 299 (2018).
 - [27] S. L. Johnson, P. Beaud, E. Vorobeva, C. J. Milne, E. D. Murray, S. Fahy, and G. Ingold, Directly observing squeezed phonon states with femtosecond x-ray diffraction, *Phys. Rev. Lett.* **102**, 175503 (2009).
 - [28] E. S. Zijlstra, A. Kalitsov, T. Zier, and M. E. Garcia, Squeezed thermal phonons precure nonthermal melting of silicon as a function of fluence, *Phys. Rev. X* **3**, 011005 (2013).
 - [29] T. K. Cheng, J. Vidal, H. J. Zeiger, G. Dresselhaus, M. S. Dresselhaus, and E. P. Ippen, Mechanism for displacive excitation of coherent phonons in sb, bi, te, and ti₂o₃, *Appl. Phys. Lett.* **59**, 1923 (1991).
 - [30] M. Hase, M. Kitajima, A. M. Constantinescu, and H. Petek, The birth of a quasiparticle in silicon observed in time–frequency space, *Nature* **426**, 51 (2003).
 - [31] J. Tersoff, New empirical model for the structural properties of silicon, *Phys. Rev. Lett.* **56**, 632 (1986).
 - [32] F. H. Stillinger and T. A. Weber, Computer simulation of local order in condensed phases of silicon, *Phys. Rev. B* **31**, 5262 (1985).
 - [33] D. Alfè and M. J. Gillan, Exchange-correlation energy and the phase diagram of Si, *Phys. Rev. B* **68**, 205212 (2003).
 - [34] K. Yamaguchi and K. Itagaki, Measurement of high temperature heat content of silicon by drop calorimetry, *Journal of Thermal Analysis and Calorimetry* **69**, 1059 (2002).
 - [35] A. Jayaraman, W. Klement, and G. C. Kennedy, Melting and polymorphism at high pressures in some group iv elements and iii-v compounds with the diamond/zincblende structure, *Phys. Rev.* **130**, 540 (1963).
 - [36] F. Dorner, Z. Sukurma, C. Dellago, and G. Kresse, Melting si: Beyond density functional

- theory, *Phys. Rev. Lett.* **121**, 195701 (2018).
- [37] B. Ramberger, T. Schäfer, and G. Kresse, Analytic interatomic forces in the random phase approximation, *Phys. Rev. Lett.* **118**, 106403 (2017).
- [38] T. Kumagai, S. Izumi, S. Hara, and S. Sakai, Development of bond-order potentials that can reproduce the elastic constants and melting point of silicon for classical molecular dynamics simulation, *Computational Materials Science* **39**, 457 (2007).
- [39] P. Koblinski, M. Z. Bazant, R. K. Dash, and M. M. Treacy, Thermodynamic behavior of a model covalent material described by the environment-dependent interatomic potential, *Phys. Rev. B* **66**, 064104 (2002).
- [40] H. C. Andersen, Molecular dynamics simulations at constant pressure and/or temperature, *The Journal of Chemical Physics* **72**, 2384 (1980).
- [41] W. C. Swope, H. C. Andersen, P. H. Berens, and K. R. Wilson, A computer simulation method for the calculation of equilibrium constants for the formation of physical clusters of molecules: Application to small water clusters, *The Journal of Chemical Physics* **76**, 637 (1982).
- [42] V. P. Lipp, B. Rethfeld, M. E. Garcia, and D. S. Ivanov, Atomistic-continuum modeling of short laser pulse melting of si targets, *Phys. Rev. B* **90**, 245306 (2014).